JOURNAL OF SYNCHROTRON RADIATION

ISSN 1600-5775

Covalency between the uranyl ion and dithiophosphinate by sulfur *K*-edge X-ray absorption spectroscopy and density functional theory

Yusheng Zhang,[a] Wuhua Duan,[a] Qiang Wang,[a] Lei Zheng,[b] Jianchen Wang,[a] Jing Chen[a] and Taoxiang Sun[a]*

[a]Institute of Nuclear and New Energy Technology, Tsinghua University, Beijing 100084, People's Republic of China, and [b]Institute of High Energy Physics, Chinese Academy of Sciences, Beijing 100049, People's Republic of China.
*Correspondence e-mail: sunstx@tsinghua.edu.cn

Received 19 August 2021
Accepted 10 November 2021

Edited by S. Wang, Soochow University, People's Republic of China

Keywords: covalency; uranyl ion; dithiophosphinate; X-ray absorption spectroscopy; density functional theory.

Supporting information: this article has supporting information at journals.iucr.org/s

The dithiophosphinic acids (HS_2PR_2) have been used for the selective separation of trivalent actinides (An^{III}) from lanthanides (Ln^{III}) over the past decades. The substituents on the dithiophosphinic acids dramatically impact the separation performance, but the mechanism is still open for debate. In this work, two dithiophosphinic acids with significantly different An^{III}/Ln^{III} separation performance, *i.e.* diphenyl dithiophosphinic acid (HS_2PPh_2) and bis(*ortho*-trifluoromethylphenyl) dithiophosphinic acid [$HS_2P(o\text{-}CF_3C_6H_4)_2$], are employed to understand the substituent effect on the bonding covalency between the $S_2PR_2^-$ anions (R = Ph and o-$CF_3C_6H_4$) and the uranyl ion by sulfur *K*-edge X-ray absorption spectroscopy (XAS) in combination with density functional theory calculations. The two $UO_2(S_2PR_2)(EtOH)$ complexes display similar XAS spectra, in which the first pre-edge feature with an intensity of 0.16 is entirely attributed to the transitions from S 1*s* orbitals to the unoccupied molecular orbitals due to the mixing between U 5*f* and S 3*p* orbitals. The Mulliken population analysis indicates that the amount of % S 3*p* character in these orbitals is essentially identical for the $UO_2(S_2PPh_2)_2(EtOH)$ and $UO_2[S_2P(o\text{-}CF_3C_6H_4)_2]_2(EtOH)$ complexes, which is lower than that in the U 6*d*-based orbitals. The essentially identical covalency in U—S bonds for the two $UO_2(S_2PR_2)_2(EtOH)$ complexes are contradictory to the significantly different An^{III}/Ln^{III} separation performance of the two dithiophosphinic acids, thus the covalency seems to be unable to account for substituent effects in the An^{III}/Ln^{III} separation by the dithiophosphinic acids. The results in this work provide valuable insight into the understanding of the mechanism in the An^{III}/Ln^{III} separation by the dithiophosphinic acids.

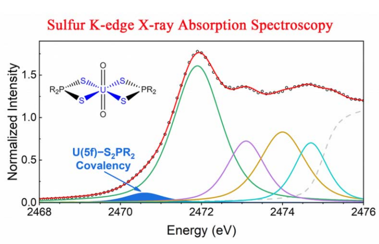

1. Introduction

The selective separation of trivalent actinides (An^{III}) and lanthanides (Ln^{III}) is one of the most urgent issues for the implementation of the partitioning and transmutation strategy within advanced nuclear fuel cycles, and it is also recognized as a critical challenge in separation science due to the almost identical ionic radii as well as the similar chemical and physical properties between An^{III} and Ln^{III}. Soft-donor ligands have demonstrated good performance in An^{III}/Ln^{III} separation, in which the dithiophosphinic acids (HS_2PR_2) show great potential in the An^{III}/Ln^{III} separation process (Bessen *et al.*, 2020). For example, bis(2,4,4-trimethylpentyl)dithiophosphinic acid (the purified Cyanex301) in kerosene can extract Am^{III} from Eu^{III} with a separation factor as high as 5000 (Chen *et al.*, 1996, 2014). Other dithiophosphinic acids with different substituents were also reported for the An^{III}/Ln^{III} separation studies (Peterman *et al.*, 2009, 2010; Xu *et al.*, 2008; Wang, Jia, Pan *et al.*, 2013; Pu *et al.*, 2019, 2020; Wang *et* *al.*, 2013, 2019). Strikingly, bis(*ortho*-trifluoromethylphenyl) dithiophosphinic acid [$HS_2P(o\text{-}CF_3C_6H_4)_2$] can afford an Am^{III}/Eu^{III} separation factor higher than 10^4, which is three orders of magnitude higher than that for diphenyl dithiophosphinic acid (HS_2PPh_2) (Xu *et al.*, 2008; Peterman *et al.*, 2010).

Several factors emerged in the previous studies that are responsible for the substituent effect in the An^{III}/Ln^{III} separation by the dithiophosphinic acids, including (1) the deprotonation properties of the dithiophosphinic acids (Wang *et al.*, 2019; Pu *et al.*, 2020), (2) the chemical stoichiometry and structure of the extracted complexes (Pu *et al.*, 2020; Xu & Rao, 2014; Greer *et al.*, 2020; Tian *et al.*, 2002, 2003; Weigl *et al.*, 2005), and (3) the difference in the binding affinity of the ligands to the metals (especially the covalent part) (Keith & Batista, 2012; Lan *et al.*, 2012; Cao *et al.*, 2010; Bhattacharyya *et al.*, 2011). For instance, the unexpectedly high pK_a and strong nucleophile for $HS_2P(o\text{-}CF_3C_6H_4)_2$ may destabilize the anion to a greater extent and increase selectivity towards actinides (Benson *et al.*, 2008; Leavitt *et al.*, 2008). Pu *et al.* found that $S_2PPh_2^-$ formed up to 2:1 complexes with Nd^{3+}, whilst $S_2P(o\text{-}CF_3C_6H_4)_2^-$ formed up to 3:1 complexes (Pu *et al.*, 2020). The substituent effect on the bonding covalency between the dithiophosphinate ligands and metal ions has been raised as an important factor in driving An^{III}/Ln^{III} separation (Keith & Batista, 2012; Daly, Keith, Batista, Boland, Clark *et al.*, 2012; Daly, Keith, Batista, Boland, Kozimor *et al.*, 2012). Daly *et al.* examined the electronic structure of several $S_2PR_2^-$ anions and found that the $S_2P(o\text{-}CF_3C_6H_4)_2^-$ anion was a 'softer' extractant as compared with the $S_2PPh_2^-$ anion, which promoted the selectivity towards actinides (Daly, Keith, Batista, Boland, Clark *et al.*, 2012). Despite the numerous theoretical calculations on modeling the extraction of Ln^{III} and An^{III} by the dithiophosphinic acids (Greer *et al.*, 2020; Lan *et al.*, 2012; Bhattacharyya *et al.*, 2011; Diamond *et al.*, 1954; Choppin, 2002; Ingram *et al.*, 2008; Gaunt *et al.*, 2008; Sadhu & Dolg, 2019; Kaneko & Watanabe, 2018; Kaneko *et al.*, 2017; Cross *et al.*, 2016; Kaneko *et al.*, 2015; Jensen & Bond, 2002; Lehman-Andino *et al.*, 2019), experimental evaluation on the covalency in M—S (where M is a metal) chemical bonding in the dithiophosphinate complexes, to the best of our knowledge, has not been reported up to now.

In this work, we are motivated to address whether the extent of covalency in the M—S bonds would account for the separation performance. The technique of ligand K-edge XAS in combination with density functional theory (DFT) calculations is employed. The intensity of the pre-edge features in XAS directly reflects the amount of ligand p character in metal-derived molecular orbitals (MOs) and thus the covalency in metal–ligand bonds (Solomon *et al.*, 2005). This technique has proven to be one of the most versatile and direct spectroscopic techniques to directly probe the mixing of metal d and f orbitals with ligand p orbitals (Kozimor *et al.*, 2008, 2009; Minasian *et al.*, 2012, 2013, 2014, 2017; Spencer *et al.*, 2013; Löble *et al.*, 2015; Pemmaraju *et al.*, 2014; Ha *et al.*, 2017; Cross *et al.*, 2017; Donahue *et al.*, 2014; Su *et al.*, 2018; Lee *et al.*, 2019; Smiles *et al.*, 2020; Sun *et al.*, 2010; Sarangi *et al.*, 2007; Queen *et al.*, 2013). As the direct examination of complexes of the trivalent actinide such as Am^{III} by synchrotron XAS is not feasible due to high radioactivity, in this work we examined the $UO_2(S_2PR_2)_2(EtOH)$ (R = Ph, o-$CF_3C_6H_4$) complexes by sulfur K-edge XAS to detect the substituent effect on the bonding covalency between the dithiophosphinate anions and the uranyl ion. Results in this work will be informative in terms of the substituent effect on the bonding covalency between the dithiophosphinate anions and trivalent actinides, and thus helpful for the understanding of the mechanism in the An^{III}/Ln^{III} separation by the dithiophosphinic acids.

2. Results and discussion

2.1. Sample preparation

Complexes of UO_2^{2+} with $S_2PR_2^-$ (R = Ph, o-$CF_3C_6H_4$) ligands were prepared and isolated as highly pure crystalline solids before the XAS experiments. Note that the complexes of UO_2^{2+} with the $S_2PPh_2^-$ ligand have been crystalized previously (Meng *et al.*, 2018; Pinkerton *et al.*, 1997; Storey *et al.*, 1983). However, the crystal structures of the complexes of UO_2^{2+} with the $S_2P(o\text{-}CF_3C_6H_4)_2^-$ ligand have not been reported. In this work, we successfully synthesized single crystals of UO_2^{2+} with the two $S_2PR_2^-$ ligands. The crystal structures of the $UO_2(S_2PR_2)_2(EtOH)$ complexes are shown in Fig. 1. Data collection and refinement details are available in Table S1 of the supporting information. Both the two $S_2PR_2^-$

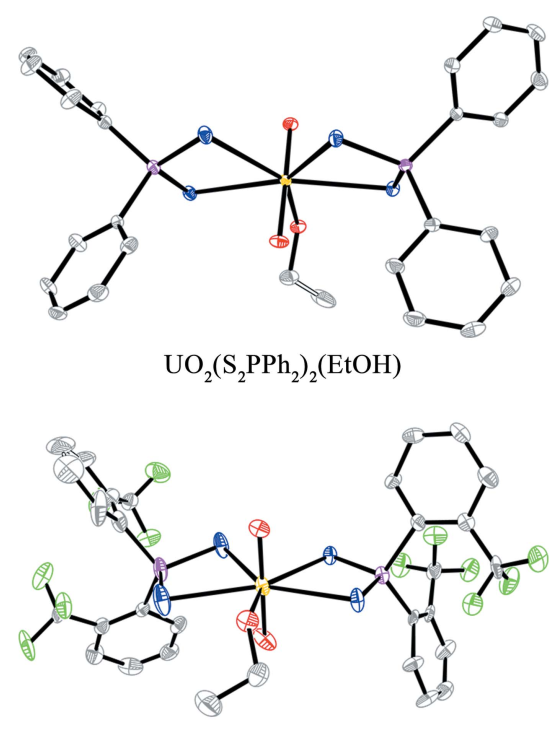

Figure 1
Crystal structure of $UO_2(S_2PR_2)_2(EtOH)$ investigated in this work with thermal ellipsoids drawn at the 30% probability level. H atoms have been omitted for clarity. (U: yellow; S: blue; P: pink; O: red; C: white; F: green.)

Table 1
Selected bond lengths (Å) and bond angles (°) for $[PPh_4][S_2PR_2]$ and $UO_2(S_2PR_2)_2(EtOH)$ in the crystal structures.

	Bond length			Bond angle		
Compound	U—O$_{yl}$	U—S	P—S	O—U—O	S—U—S	S—P—S
$[PPh_4][S_2PPh_2]$	–	–	1.977 (1)	–	–	117.80 (4)
$[PPh_4][S_2P(o\text{-}CF_3C_6H_4)_2]$	–	–	1.979 (2)	–	–	116.79 (3)
$UO_2(S_2PPh_2)_2(EtOH)$	1.765 (1)	2.863 (29)	2.010 (26)	175.77 (10)	70.74 (2)	111.09 (5)
$UO_2[S_2P(o\text{-}CF_3C_6H_4)_2]_2(EtOH)$	1.740 (42)	2.858 (36)	2.010 (11)	177.1 (10)	70.23 (19)	109.78 (93)

ligands form up to 2:1 complexes with UO_2^{2+}, similar to previous reports (Meng *et al.*, 2018; Pinkerton *et al.*, 1997; Storey *et al.*, 1983). Both the two $UO_2(S_2PR_2)_2(EtOH)$ complexes contain four sulfur atoms from the two bidentate dithiophosphinate ligands and one oxygen atom from the coordinated ethanol in the first coordinated sphere of the equatorial plane of UO_2^{2+}. The crystals of the two ligands $S_2PR_2^-$ were also obtained by employing tetraphenylphosphonium (Ph_4P^+) as the cation according to the procedure reported in the literature (Daly, Klaehn *et al.*, 2012).

The selected bond lengths and bond angles for the crystal structures of the $[PPh_4][S_2PR_2]$ ligands and the $UO_2(S_2PR_2)_2$ (EtOH) complexes are provided in Table 1. The P—S bond lengths are 1.977 and 1.979 Å in $S_2PPh_2^-$ and $S_2P(o\text{-}CF_3C_6H_4)_2^-$, respectively, and these values prolong to 2.010 Å in the two $UO_2(S_2PR_2)_2(EtOH)$ complexes, suggesting comparable bonding interactions of the two $S_2PR_2^-$ ligands with the uranyl ion. The S—U—S bond angles are 70.74° and 70.23° for $UO_2(S_2Ph_2)_2(EtOH)$ and $UO_2[S_2P(o\text{-}CF_3C_6H_4)_2]_2(EtOH)$, respectively, and the S—P—S bond angles are 111.09° and 109.78° for $UO_2(S_2PPh_2)_2(EtOH)$ and $UO_2[S_2P(o\text{-}CF_3C_6H_4)_2]_2(EtOH)$, respectively. The comparable S—U—S and S—P—S bond angles suggest comparable bonding interactions of $S_2PPh_2^-$ and $S_2P(o\text{-}CF_3C_6H_4)_2^-$ with the uranyl ion.

2.2. P *K*-edge XAS

Before the collection of S *K*-edge XAS, we collected the P *K*-edge XAS spectra for the $[PPh_4][S_2PR_2]$ ligands and the $UO_2(S_2PR_2)_2(EtOH)$ complexes. The background-subtracted and normalized P *K*-edge XAS spectra are shown in Fig. 2, and the full spectra are presented in Fig. S1 of the supporting information. The spectrum of PPh_4Cl was also collected to compare with the spectra of the $[PPh_4][S_2PR_2]$ ligands. According to the second derivatives (Fig. S2), the spectrum of PPh_4Cl contains three pre-edge features at 2147.6, 2149.4 and 2150.7 eV. The spectra of the $[PPh_4][S_2PR_2]$ ligands both contain four pre-edge features at about 2147.6, 2149.2 and 2149.8, 2150.5 eV. The spectra of the $UO_2(S_2PR_2)_2(EtOH)$ complexes both contain three pre-edge features at about 2147.6, 2148.9 and 2150 eV. The P *K*-edge XAS spectra are not very informative for the bonding interactions between the uranyl ion and the dithiophosphinate, thus collections of the S *K*-edge XAS proceeded for both the $[PPh_4][S_2PR_2]$ ligands and the $UO_2(S_2PR_2)_2(EtOH)$ complexes.

2.3. S *K*-edge XAS

The normalized and background-subtracted S *K*-edge XAS spectra of the $[PPh_4][S_2PR_2]$ (R = Ph, $o\text{-}CF_3C_6H_4$) ligands and the $UO_2(S_2PR_2)_2(EtOH)$ complexes are shown in Fig. 3. According to the second derivatives (Fig. S4), the spectrum of $[PPh_4][S_2PPh_2]$ contains three pre-edge features at 2471.3, 2472.4 and 2473.6 eV, and the spectrum of $[PPh_4][(S_2P(o\text{-}CF_3C_6H_4)_2]$ contains four pre-edge features at 2471.3, 2472.4, 2473.4 and 2474.3 eV. This result is in agreement with the previous observations by Daly and co-workers, except that

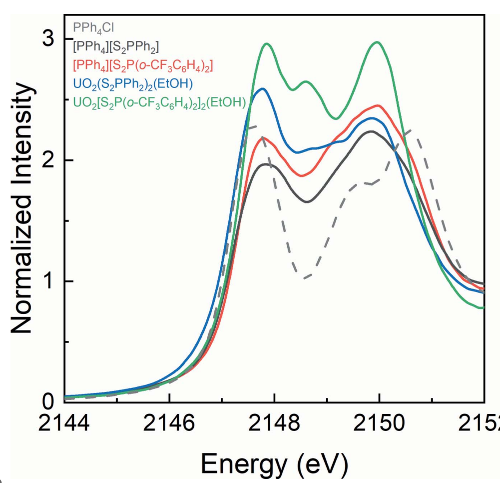

Figure 2
Background-subtracted and normalized P *K*-edge XAS spectra for PPh_4Cl, $[PPh_4][S_2PR_2]$ and $UO_2(S_2PR_2)_2(EtOH)$.

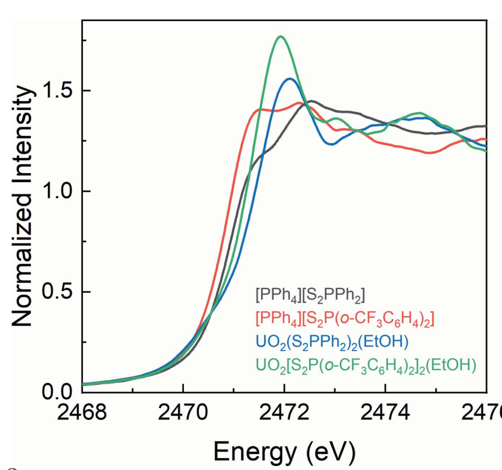

Figure 3
Comparison of the S *K*-edge XAS spectra of $[PPh_4][S_2PR_2]$ and $UO_2(S_2PR_2)_2(EtOH)$.

there is no small contribution to the spectra (>2480 eV) from sulfate contaminant (Fig. S3) (Daly, Keith, Batista, Boland, Clark *et al.*, 2012). The pre-edge features in the spectra of the $[PPh_4][S_2PR_2]$ ligands can be assigned to electron transitions from S 1*s* orbitals to the aryl C_π^* orbitals containing small amounts of sulfur 3*p* character, P—S σ^* and P—S $\sigma^* + \pi^*$ orbitals (Daly, Keith, Batista, Boland, Clark *et al.*, 2012). Compared with the spectra of $[PPh_4][S_2PR_2]$, the two $UO_2(S_2PR_2)$ (EtOH) complexes display pre-edge features around 2472.0, 2473.5 and 2474.8 eV and also contain a shoulder feature at about 2470.5 eV (Fig. S5). This shoulder feature in the S *K*-edge XAS of the $UO_2(S_2PR_2)_2$(EtOH) complexes is ascribed to the covalent interaction between the uranyl ion and the $S_2PR_2^-$ ligands.

To quantify the intensities of the pre-edge features, the S *K*-edge XAS spectra of the $UO_2(S_2PR_2)_2$(EtOH) complexes were modeled using pseudo-Voigt functions with a 1:1 ratio of Lorentzian and Gaussian function contributions and a step function with a 1:1 ratio of arctangent and error function contributions. The energy positions of the features determined by the second derivatives are fixed during the curve-fits (Figs. S5 and S6). The curve-fits parameters are summarized in Table S2.

The pre-edge region in the spectrum of $UO_2(S_2PPh_2)_2$ (EtOH) is best modeled by four pseudo-Voigt functions at 2470.5, 2472.0, 2473.5 and 2474.8 eV, and that of $UO_2[S_2P(o\text{-}CF_3C_6H_4)_2]_2$(EtOH) by five pseudo-Voigt functions at 2470.6, 2471.9, 2473.1, 2474.0 and 2474.7 eV, as shown in Fig. 4 and Table 2. Note that the shoulder at the energy of 2470.5 eV and 2470.6 eV are both 0.16 of the intensity for $UO_2(S_2Ph_2)_2$(EtOH) and $UO_2[S_2P(o\text{-}CF_3C_6H_4)_2)]_2$(EtOH). Resembling the spectra of $[PPh_4][S_2PR_2]$, the fourth feature observed in the spectrum of $UO_2(S_2PPh_2)_2$(EtOH) at 2474.8 eV splits into two features at 2474.0 and 2474.7 eV in the spectrum of $UO_2[S_2P(o\text{-}CF_3C_6H_4)_2]_2$(EtOH), which may be attributed to the orbital splitting resulting from symmetry change and nonuniform C—P—S angles, according to the results reported by Daly and co-workers (Daly, Keith, Batista, Boland, Clark *et al.*, 2012).

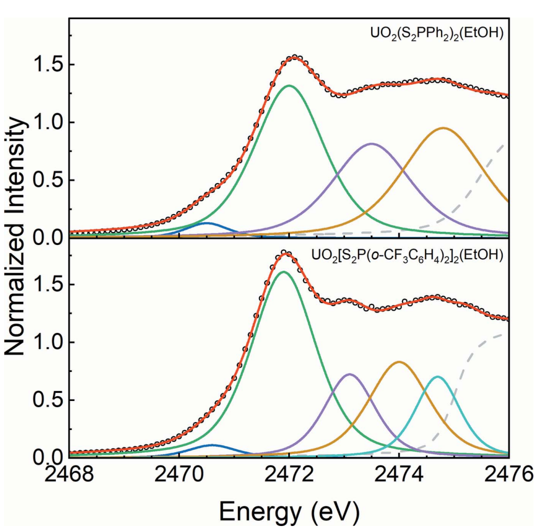

Figure 4
Curve-fitting results of S *K*-edge XAS for $UO_2(S_2PR_2)_2$(EtOH). The experimental data are shown by black circles, and the total curve fits are shown by red traces. Post-edge residuals (dashed gray traces) are generated by subtracting the pre-edge pseudo-Voigt functions (blue, green, purple, yellow, light blue) from the total curve fits.

Table 2
The energy and intensity obtained by curve-fitting of the S *K*-edge XAS for $UO_2(S_2PR_2)_2$.

Compound	Energy (eV)	Intensity
$UO_2(S_2PPh_2)_2$(EtOH)	2470.5	0.16
	2472.0	2.65
	2473.5	1.85
	2474.8	2.26
$UO_2[S_2P(o\text{-}CF_3C_6H_4)_2]_2$(EtOH)	2470.6	0.16
	2471.9	2.99
	2473.1	1.05
	2474.0	1.46
	2474.7	0.89

2.4. DFT and time-dependent DFT (TDDFT) calculations

The electronic structure of the $S_2PR_2^-$ anions has been deeply investigated by Daly and co-workers, revealing that the S 3*p* orbitals mix with P 3*p* orbitals to form two σ-type and one π-type P—S bonds in the S_2P^- moiety of $S_2PR_2^-$, and the orbitals of the S_2P^- moiety mix with the σ- and π-type orbitals of the aryl groups (Daly, Keith, Batista, Boland, Clark *et al.*, 2012; Daly, Keith, Batista, Boland, Kozimor *et al.*, 2012). Therefore, the $S_2PR_2^-$ ligands can provide both σ and π orbitals to interact with the uranyl ion in the $UO_2(S_2PR_2)_2$(EtOH) complexes.

The involvement of both U 5*f* and 6*d* orbitals in the covalent bonds between uranium and axial oxygen (O_{yl}) atoms induces a geometrically linear and redox-stable uranyl ion (Denning, 1992, 2007; Denning *et al.*, 2002; Cowie *et al.*, 2019), around which other ligands are confined to the equatorial plane to interact with the U 5*f* and 6*d* orbitals. DFT calculations were employed to account for the XAS spectra of the $UO_2(S_2PR_2)_2$(EtOH) complexes in this work. The energy level diagram of the truncated unoccupied MOs for the two $UO_2(S_2PR_2)_2$(EtOH) complexes is presented in Fig. 5, and has been shifted by a constant to ensure the energies of the S 1*s* orbitals are equivalent to each other, in order to directly compare with the S *K*-edge XAS. The U 5*f*- and 6*d*-dominant MOs are shown by red and blue lines, respectively. There are four orbitals (1–4a) belonging to the σ- and π-type mixing of the S_2P orbitals with U 5*f* orbitals near −3 eV, and the contours of these four orbitals are illustrated in Fig. 6. Other U 5*f*-dominant MOs locate around −1.25 eV showing the orbital mixing between U 5*f* and S 3*p* orbitals, blending in with some orbitals (black lines, ranging from −1.5 eV to −0.5 eV) that contain significant phenyl character (C_π^*) and only small contributions from S_2P fragment orbitals. The U 6*d*-dominant MOs (5–9a, blue lines) are distributed ranging from −0.5 eV to 2.0 eV, interspersing with some σ^* S_2P orbitals (gray lines) containing little S 3*p* character. The contours of the U 6*d*-dominant MOs (5–9a) for $UO_2(S_2PR_2)_2$(EtOH) are illustrated

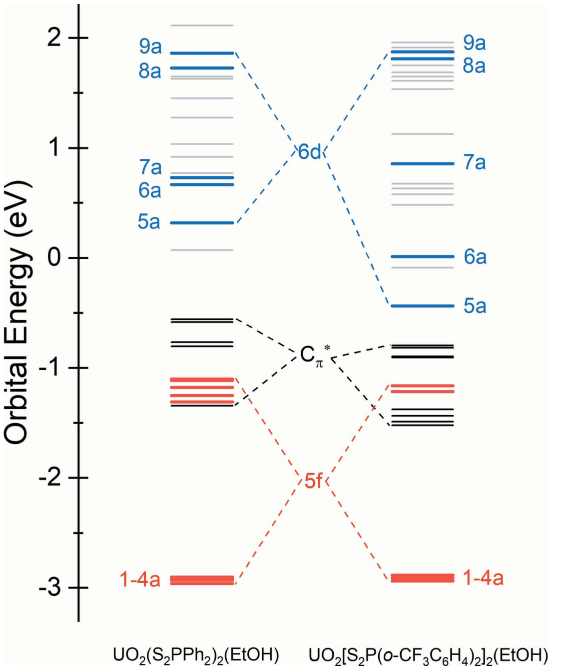

Figure 5
The truncated orbitals energy levels for $UO_2(S_2PR_2)_2(EtOH)$ calculated at the B3LYP/TZ2P level. The red and blue lines denote the orbitals containing primarily U 5*f* and 6*d* character, respectively.

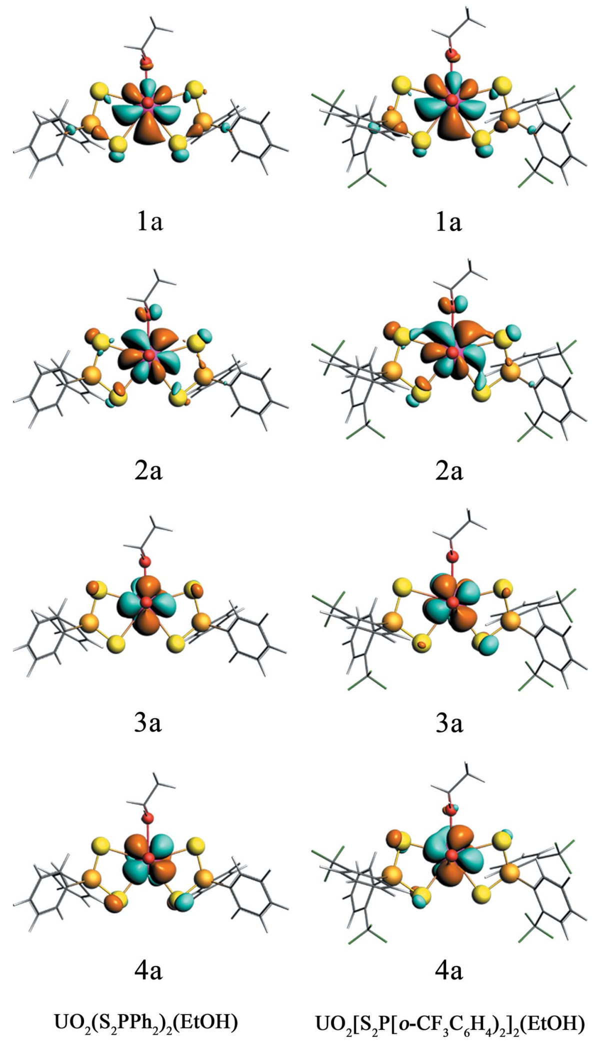

Figure 6
The contours of unoccupied Kohn–Sham orbitals (1–4a) containing primarily U 5*f* character for $UO_2(S_2PR_2)_2(EtOH)$ in 0.02 a.u.

in Fig. 7, and those of the orbitals containing significant phenyl character (C_π^*) for $UO_2(S_2PR_2)_2(EtOH)$ are illustrated in Fig. S7.

According to the orbital energies obtained by the ground-state DFT calculations in Fig. 5, the first pre-edge features around 2470.5 eV in the S *K*-edge XAS of the $UO_2(S_2PR_2)_2(EtOH)$ complexes in Fig. 4 are reasonably assigned to the transitions from S 1*s* orbitals to the U 5*f*-dominant MOs (1–4a). The second pre-edge features around 2472.0 eV are dominated by the transitions associated with primarily phenyl character (C_π^*). The other pre-edge features at energy from 2473 to 2475 eV are contributed by U 6*d*-dominant MOs and orbitals containing little S 3*p* components without U 5*f* or 6*d* character.

The S *K*-edge XAS spectra for the $UO_2(S_2PR_2)_2(EtOH)$ complexes were simulated by TDDFT calculations to directly compare with the experiment XAS (Fig. 8). The simulated spectra for both $UO_2(S_2PR_2)_2(EtOH)$ complexes have been shifted by +49.7 eV to account for the omission of the atomic and extra-atomic relaxation associated with the core excitation, relativistic stabilization, and errors associated with the functional (Martin & Shirley, 1977; Segala & Chong, 2010).

The simulated spectra are in good agreement with the experimental spectra. The transitions around 2470.5 eV in the simulated spectra are observed for both the $UO_2(S_2PR_2)_2(EtOH)$ complexes, which is entirely attributed to the transitions from S 1*s* orbitals to the U 5*f*-dominant unoccupied MOs (1–4a), indicating the covalent mixing between S 3*p* orbitals and U 5*f* orbitals. The transitions from S 1*s* orbitals to the primarily phenyl character (C_π^*) unoccupied MOs and little U 5*f* character unoccupied MOs both contribute to the pre-edge features around 2472.0 eV obtained by curve-fits in Fig. 4. The other pre-edge features above 2473 eV are associated with the transitions to the U 6*d*-dominant MOs and to the orbitals containing little S 3*p* components without U 5*f* or 6*d* character.

2.5. Evaluation of the bonding covalency between the uranyl ion and the $S_2PR_2^-$ ligands

It has been well known that the amount of ligand *np* character in metal-derived MOs can be determined from the intensities observed in the pre-edge features in the ligand *K*-edge XAS (Solomon *et al.*, 2005; Barton *et al.*, 2015). Generally, an intensity standard is used to convert the experimental intensity of a pre-edge feature to the amount of ligand *np* character in metal–ligand bonds. For example, an intensity of 0.53 = 7.5% Cl 3*p*-character per bond obtained from Cs_2CuCl_4 is used as the Cl *K*-edge XAS intensity standard (Solomon *et al.*, 2005). The standards for thiolate (SR^-) (Shadle *et al.*, 1993), sulfide (S^{2-}) (Rose *et al.*, 1999) and enedithiolate

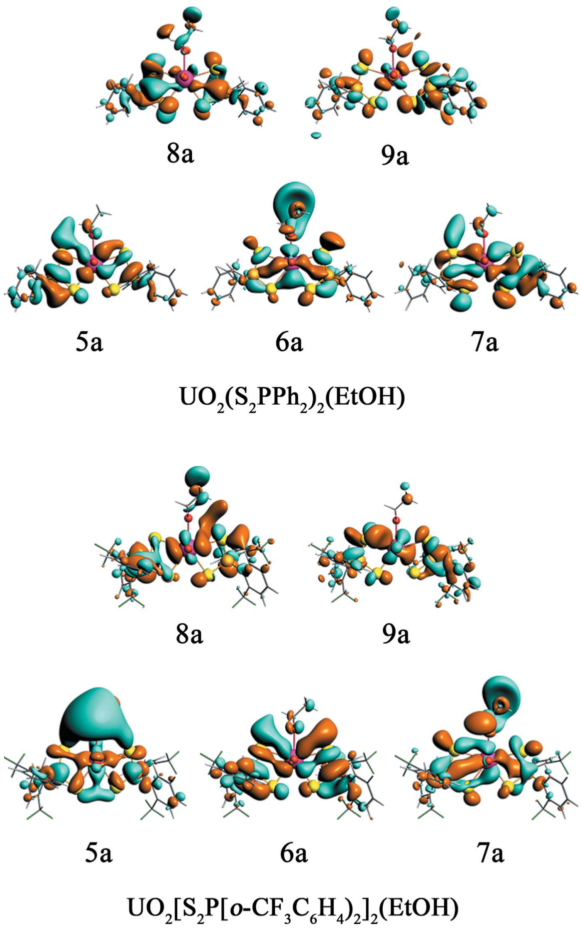

Figure 7
The contours of unoccupied Kohn–Sham orbitals (5–9a) containing primarily U 6*d* character for $UO_2(S_2PR_2)_2(EtOH)$ in 0.02 a.u.

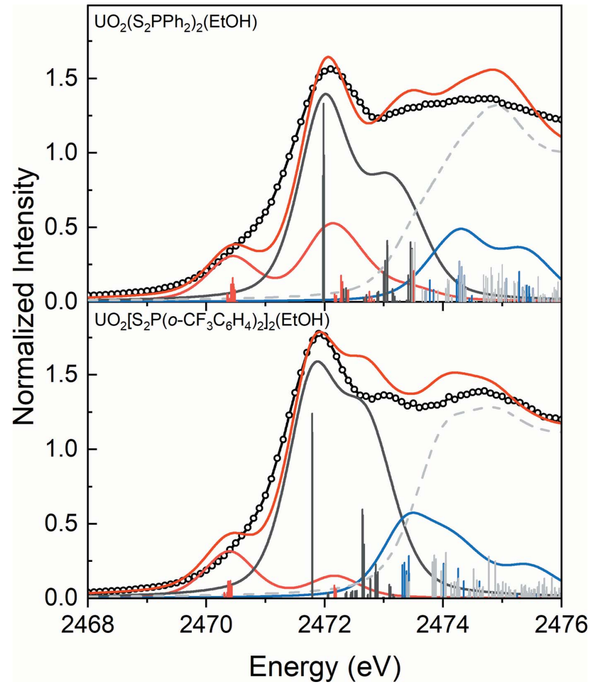

Figure 8
Comparison of the simulated spectra obtained by calculations (red) with the experimental S *K*-edge XAS data for $UO_2(S_2PR_2)_2(EtOH)$ (black). The purple, blue, orange and light gray bars represent the energies and oscillator strengths for the calculated transitions involving U 5*f*, 6*d*, C_π^* and S_2P orbitals containing little S 3*p* character without U 5*f* or 6*d* character, respectively.

($S_2R_2^{2-}$) (Szilagyi *et al.*, 2003) have been established to evaluate the amount of S 3*p* character in *M*—S bonds. Since the intrinsic transition dipole for the S 1*s* → 3*p* excitation is dependent on the effective nuclear charge Z_{eff} (S) for each S-ligand (Solomon *et al.*, 2005), it is not appropriate to directly use the standard for thiolate, sulfide or enedithiolate to convert the intensities in this work (S in the form of $S_2PR_2^-$) to % S 3*p* character. Therefore, we herein use the data from Mulliken population analysis that are associated with the experimental XAS data to evaluate the bonding covalency between the uranyl ion and the $S_2PR_2^-$ ligands (Table 3).

The DFT calculations show that the amount of S 3*p* character in the U 5*f*-dominant unoccupied MOs of 1a, 2a, 3a and 4a for $UO_2(S_2PPh)_2(EtOH)$ is 2.68%, 3.75%, 1.95% and 3.04%, respectively. For $UO_2\{[S_2P(o\text{-}CF_3C_6H_4)]_2\}_2(EtOH)$, these values are 1.95%, 4.09%, 2.48% and 2.73%, respectively. The total amount of S 3*p* character of the orbitals of 1a, 2a, 3a and 4a are 11.42% and 11.25%, corresponding to 2.86% and 2.81% per U—S bond in $UO_2(S_2PPh)_2(EtOH)$ and $UO_2\{[S_2P(o\text{-}CF_3C_6H_4)]_2\}_2(EtOH)$, respectively. The DFT calculations also show that the amount of S 3*p* character in the U 6*d*-dominant unoccupied MOs of 5a, 6a, 7a, 8a and 9a for $UO_2(S_2PPh)_2(EtOH)$ is 12.11%, 9.0%, 13.43%, 14.43% and 16.78%, respectively. For $UO_2[(S_2P(o\text{-}CF_3C_6H_4))_2]_2(EtOH)$, these values are 13.00%, 21.93%, 8.94%, 6.29% and 13.39%, respectively. The average amount of S 3*p* character in U 6*d*-based orbitals (5–9a) obtained from the DFT calculations are 13.15% and 12.71% for $UO_2(S_2PPh)_2(EtOH)$ and $UO_2\{[S_2P(o\text{-}CF_3C_6H_4)]_2\}_2(EtOH)$, respectively, thus the S 3*p* orbitals are engaged more in the U 6*d* orbitals than that in the U 5*f* orbitals, consistent with the previous reports that the 6*d* orbitals play a significant role in actinide bonding relative to the 5*f* orbitals (Minasian *et al.*, 2012; Pepper & Bursten, 1991; Su *et al.*, 2018; Cross *et al.*, 2017). The average amount of S 3*p* character in the orbitals with primarily phenyl character (C_π^*) obtained from the DFT calculations is 2.25% and 3.65% for $UO_2(S_2PPh)_2(EtOH)$ and $UO_2\{[S_2P(o\text{-}CF_3C_6H_4)]_2\}_2(EtOH)$, respectively, indicating an important contribution to the pre-edge features. Although only the first pre-edge feature around 2470.5 eV in each spectrum is exclusively attributed to the transitions from S 1*s* orbitals to the U 5*f*-dominant unoccupied MOs (1–4a), the XAS data and DFT calculations both suggest that the mixing of U 5*f* and 6*d* orbitals with S 3*p* orbitals are similar in the two $UO_2(S_2PR_2)_2(EtOH)$ complexes, indicating that introduction of *o*-CF_3 into phenyl has little effect on the covalent bonding between $S_2PR_2^-$ and UO_2^{2+}.

3. Conclusion

A combination of the S *K*-edge XAS technique and DFT calculations has been conducted on $UO_2(S_2PR_2)_2(EtOH)$ (*R* = Ph and *o*-$CF_3C_6H_4$) complexes to obtain direct insight into the

Table 3
Mulliken population analysis for unoccupied MOs of the $UO_2(S_2PR_2)_2(EtOH)$.

Compound	MO		Energy (eV)	% S 3*p*	% S 3*p* average
$UO_2(S_2PPh_2)_2(EtOH)$	5*f*	1a	−2.96	2.68	2.86
		2a	−2.93	3.75	
		3a	−2.91	1.95	
		4a	−2.90	3.04	
	6*d*	5a	0.32	12.11	13.15
		6a	0.67	9.00	
		7a	0.73	13.43	
		8a	1.73	14.43	
		9a	1.86	16.78	
	C_π^*	10a	−1.34	9.25	2.25
		11a	−0.80	0.39	
		12a	−0.77	0.62	
		13a	−0.59	0.51	
		14a	−0.56	0.50	
$UO_2[S_2P(o\text{-}CF_3C_6H_4)_2]_2(EtOH)$	5*f*	1a	−3.30	1.95	2.81
		2a	−3.27	4.09	
		3a	−3.25	2.48	
		4a	−3.24	2.73	
	6*d*	5a	−0.80	13.00	12.71
		6a	−0.35	21.93	
		7a	0.50	8.94	
		8a	1.45	6.29	
		9a	1.51	13.39	
	C_π^*	10a	−1.88	6.95	3.65
		11a	−1.85	4.78	
		12a	−1.80	6.15	
		13a	−1.74	5.48	
		14a	−1.27	0.73	
		15a	−1.26	0.80	
		16a	−1.18	2.77	
		17a	−1.16	1.54	

contributions of U 6*d* and especially 5*f* orbitals to the covalency in the U—S bonds, in order to illuminate the role of the bonding covalency in the An^{III}/Ln^{III} separation by the dithiophosphinic acids. The two $UO_2(S_2PR_2)_2(EtOH)$ complexes display similar pre-edge features in the S *K*-edge XAS, the first of which is entirely attributed to the transitions from S 1*s* orbitals to the U 5*f* orbitals mixing with the S 3*p* orbitals. Curve-fitting analysis indicates identical intensities of 0.16 for the first pre-edge feature of the two $UO_2(S_2PR_2)_2(EtOH)$ complexes. Consistently, the amounts of S 3*p* character per U—S bond for $UO_2(S_2Ph_2)_2(EtOH)$ and $UO_2[S_2P(o\text{-}CF_3C_6H_4)_2]_2(EtOH)$ by Mulliken population analysis are essentially identical to each other. In addition, the DFT calculations show that the amounts of S 3*p* character in U 6*d*-based orbitals are also nearly equivalent for the two $UO_2(S_2PR_2)_2(EtOH)$ complexes. The XAS data and DFT calculations demonstrate essentially identical bonding covalency in the two $UO_2(S_2PR_2)_2(EtOH)$ complexes, indicating that the introduction of *o*-CF_3 into phenyl has little effect on the covalent bonding between the $S_2PR_2^-$ ligands and UO_2^{2+}. The essentially identical covalency in the U—S bonds for the two $UO_2(S_2PR_2)_2(EtOH)$ complexes are contradictory to the significantly different An^{III}/Ln^{III} separation performance of the two dithiophosphinic acids. The *M*—S bonding covalency seems to be unable to account for the substituent effect in the An^{III}/Ln^{III} separation by the dithiophosphinic acids. According to the results in the previous work as mentioned in the *Introduction*, we speculate that the different chemical stoichiometry and structure of the extracted complexes should be the main reason for the significantly different separation performance of HS_2PPh_2 and $HS_2P(o\text{-}CF_3C_6H_4)_2$ in the An^{III}/Ln^{III} separation. Nevertheless, it is worthwhile conducting an experimental investigation on the bonding covalency between the trivalent actinides and dithiophosphinate ligands with different substituents in the future.

4. Experimental section

4.1. Synthesis of $UO_2(S_2PR_2)_2(EtOH)$

All manipulations were carried out in a glove box under an atmosphere of nitrogen to rigorously exclude air and moisture. Ethanol was dried and degassed by the solvent purification system, and transferred to the glove box without exposure to air. Super dry dichloromethane was stored over activated molecular sieves prior to use. Single crystals of $[PPh_4][S_2PR_2]$ suitable for X-ray diffraction characterization were obtained by recrystallization from a 1:1 acetonitrile/toluene solution under air and at ambient conditions, according to the procedure reported in the literature (Daly, Klaehn *et al.*, 2012). In synthesizing the single crystals of the two $UO_2(S_2PR_2)_2(EtOH)$ complexes, two dithiophosphinate ligands in the ammonium form $[NH_4][S_2PR_2]$ were used according to the previous procedures (Daly, Klaehn *et al.*, 2012).

$UO_2(S_2PPh_2)_2(EtOH)$. Single crystals of the $UO_2(S_2PR_2)_2(EtOH)$ complexes were prepared using the reported procedures with slight modifications (Meng *et al.*, 2018; Pinkerton *et al.*, 1997; Storey *et al.*, 1983). A solution of $[NH_4][S_2PPh_2]$ (54.2 mg, 0.203 mmol) in ethanol (2 ml) was mixed with a solution of UO_2Cl_2 (35.8 mg) in ethanol (2 ml). The mixture was stirred for 20 min at 70°C to give an orange solution. A slight white precipitate was generated over the course of the reaction. The orange solution was taken to dryness and the resulting complexes were extracted from the white–orange solid residue with dichloromethane (10 ml). The products were recrystallized after solvent removal from 1.5 ml ethanol. After one week, single crystals suitable for X-ray diffraction were obtained at room temperature. IR (cm^{-1}, solid sample on ATR cell): 923 (asymmetric O═U═O stretching), 559 (symmetric PS_2 stretching), 631 (asymmetric PS_2 stretching). Raman (cm^{-1}): 840 (symmetric O═U═O stretching). Anal. Calcd for $C_{26}H_{26}O_3P_2S_4U$: C, 38.33; H, 3.22. Found: C, 38.24; H, 3.27.

$[UO_2[S_2P(o\text{-}CF_3C_6H_4)_2]_2(EtOH)]\cdot EtOH$. Single crystals of $UO_2[S_2P(o\text{-}CF_3C_6H_4)_2]_2(EtOH)$ were prepared as described above for $UO_2(S_2PPh_2)_2(EtOH)$ from $[NH_4][S_2P(o\text{-}CF_3C_6H_4)_2]$ (71.4 mg, 0.177 mmol) and UO_2Cl_2 (35.4 mg). IR (cm^{-1}, solid sample on ATR cell): 930 (asymmetric O═U═O stretching), 560 (symmetric PS_2 stretching), 646 (asymmetric PS_2 stretching). Raman (cm^{-1}): 845 (symmetric

O═U═O stretching). Anal. Calcd for $C_{32}H_{28}F_{12}O_4P_2S_4U$: C, 33.93; H, 2.49. Found: C, 33.79; H, 2.66.

4.2. X-ray crystallography

The single-crystal X-ray diffraction data for $[PPh_4][S_2PR_2]$ and $UO_2(S_2PR_2)_2(EtOH)$ complexes were collected on a Rigaku Super Nova, Dual, Cu at zero, AtlasS2 diffractometer. The measurements were performed with Cu/$K\alpha$ (λ = 1.54184 Å) or Mo/$K\alpha$ (λ = 0.71073 Å) radiation. All crystals were kept at 173 K during data collection. Data collection and reduction were carried out in *CrysAlisPro*, Version 1.171.39.46 (Rigaku Oxford Diffraction, 2018). A multi-scan method for absorption corrections was applied to the data sets. All the structures were solved by intrinsic phasing method and refined by full matrix least-squares techniques with anisotropic temperature factors of all non-hydrogen atoms on F^2, using the *SHELX-97* and *Olex2-1.2* program (Sheldrick, 2008; Dolomanov *et al.*, 2009). All H atoms were refined with anisotropic displacement parameters. The H atoms were placed in ideal sites and were not refined for good refinement convergence. Further data collection and refinement details are summarized in Table S1. The CIF files containing the supplementary crystallographic data for $[PPh_4][S_2PR_2]$ and $UO_2(S_2PR_2)_2(EtOH)$ are available through the Cambridge Crystallographic Data Centre (CCDC 2103608–2103611).

4.3. XAS measurements and data analysis

The S and P *K*-edge XAS measurements were conducted on beamline 4B7A of Beijing Synchrotron Radiation Facility (BSRF) over an energy range from 1750 eV to 6000 eV. The energy of the electron beam is 2.5 GeV in the storage ring with a maximum beam current of 250 mA. A beam spot tightly focused at a sample is about 1.5 mm × 0.4 mm, and the measured flux is over 3×10^{10} photons s^{-1} $(250\ mA)^{-1}$ (Zheng *et al.*, 2014). The samples were measured by partial fluorescence yield mode using a 13-element Si (Li) array detector.

For S and P *K*-edge XAS measurements, single-crystal samples were finely ground into a homogeneous powder which was dispersed as thinly as possible on the carbon tape. The energy scale in the S and P *K*-edge XAS was calibrated by using $Na_2S_2O_3$ and $Na_4P_2O_7$ standards, respectively, which was repeatedly analyzed at intervals between sample scans. All spectra were collected in duplicate at least twice to obtain adequate statistics. Spectra showed no signs of radiation damage and were reproduced over multiple regions of the sample.

Background subtraction and normalization of S and P *K*-edge XAS data were manipulated using the *Athena* interface in the *Demeter* software program (Ravel & Newville, 2005). In a typical example, a line was fit to the pre-edge region and then subtracted from the experimental data to eliminate the background of the spectrum. The data were normalized to a unit step height by fitting a second-order polynomial to the post-edge region of the spectrum. Curve-fitting of the S *K*-edge XAS was performed using the program *IGOR Pro 8.04* and a modified version of *EDG_FIT* (George, 2001). Second-derivative spectra were used as guides to determine the number and position of peaks. Pre-edge and rising edge features were modeled by symmetrically constrained pseudo-Voigt line shapes with a fixed 1:1 Lorentzian to Gaussian ratio and a step function with a 1:1 ratio of arctangent and error function, respectively. Fits were performed over several energy ranges. The quality of each curve-fit was determined by evaluating changes in χ^2 and by inspecting the residual intensity, which is obtained by subtracting the fit from the experiment data and should resemble a horizontal line at zero. The area under the pre-edge features (defined as the intensity) was used as the transition intensity.

4.4. DFT calculations

All DFT calculations were carried out with the *Amsterdam Density Functional* (*ADF 2019*) program (Baerends *et al.*, 2019; te Velde *et al.*, 2001), employing the B3LYP hybrid functional (Becke, 1988; Lee *et al.*, 1988). The all-electron Slater-type orbital (STO) basis sets of triple-ζ augmented by two sets of polarization functions (TZ2P) were adapted for the description of all atoms. The zero-order regular approximation (ZORA) approach was used to account for the scalar relativistic (SR) effects (Faas *et al.*, 1995). Mulliken population analyses were conducted on particular MOs to obtain the reported orbital populations in the two $UO_2(S_2PR_2)_2(EtOH)$ complexes (Mulliken, 1955).

The S *K*-edge XAS spectra for all complexes were simulated by TDDFT using the Davidson method. The simulated spectra were obtained by calculating core electron excitations originating from S 1*s* dominated MOs to virtual MOs at the optimized crystal structure. Only excitations from S 1*s* core levels to virtual orbitals were analyzed by restricting the energy range of core level and virtual orbitals involved in excitation. The calculated oscillator strengths were evenly broadened with a pseudo-Voigt functions with a 1:1 ratio of Lorentzian and Gaussian function contributions of 1 eV full width at half-maximum to generate the simulated absorption spectra. An energy shift of +49.7 eV was applied for the simulated spectra to account for the omission of atomic and extra-atomic relaxation associated with the core excitation, relativistic stabilization, and errors associated with the functional, according to the literature (Martin & Shirley, 1977; Segala & Chong, 2010).

Acknowledgements

We are grateful to Ming Li (Tsinghua University) for his help on single-crystal structures and Zhixian Wang (Peking University) for her help on element analysis.

Funding information

The following funding is acknowledged: National Natural Science Foundation of China (contract No. 21976103; contract No. U1830202).

References

Baerends, E. J., Ziegler, T., Autschbach, J., Bashford, D., Bérces, A., Bickelhaupt, F. M., Bo, C., Boerrigter, P. M., Cavallo, L., Chong, D. P., Deng, L., Dickson, R. M., Ellis, D. E., van Faassen, M., Fan, L., Fischer, T. H., Fonseca Guerra, C., Franchini, M., Ghysels, A., Giammona, A., van Gisbergen, S. J. A., Götz, A. W., Groeneveld, J. A., Gritsenko, O. V., Grüning, M., Gusarov, S., Harris, F. E., van den Hoek, P., Jacob, C. R., Jacobsen, H., Jensen, L., Kaminski, J. W., van Kessel, G., Kootstra, F., Kovalenko, A., Krykunov, M. V., van Lenthe, E., McCormack, D. A., Michalak, A., Mitoraj, M., Morton, S. M., Neugebauer, J., Nicu, V. P., Noodleman, L., Osinga, V. P., Patchkovskii, S., Pavanello, M., Philipsen, P. H. T., Post, D., Pye, C. C., Ravenek, W., Rodríguez, J. I., Ros, P., Schipper, P. R. T., van Schoot, H., Schreckenbach, G., Seldenthuis, J. S., Seth, M., Snijders, J. G., Solà, M., Swart, M., Swerhone, D., te Velde, G., Vernooijs, P., Versluis, L., Visscher, L., Visser, O., Wang, F., Wesolowski, T. A., van Wezenbeek, E. M., Wiesenekker, G., Wolff, S. K., Woo, T. K. & Yakovlev, A. L. (2019). *ADF2019*. SCM, Theoretical Chemistry, Vrije Universiteit, Amsterdam, The Netherlands (http://www.scm.com).

Barton, R. L., Gardenghi, D. J., Stolte, W. C. & Szilagyi, R. K. (2015). *J. Phys. Chem. A*, **119**, 5579–5586.

Becke, A. D. (1988). *Phys. Rev. A*, **38**, 3098–3100.

Benson, M. T., Moser, M. L., Peterman, D. R. & Dinescu, A. (2008). *J. Mol. Struct. Theochem*, **867**, 71–77.

Bessen, N. P., Jackson, J. A., Jensen, M. P. & Shafer, J. C. (2020). *Coord. Chem. Rev.* **421**, 213446–213461.

Bhattacharyya, A., Ghanty, T. K., Mohapatra, P. K. & Manchanda, V. K. (2011). *Inorg. Chem.* **50**, 3913–3921.

Cao, X., Heidelberg, D., Ciupka, J. & Dolg, M. (2010). *Inorg. Chem.* **49**, 10307–10315.

Chen, J., He, X. H. & Wang, J. C. (2014). *Radiochim. Acta*, **102**, 41–51.

Chen, J., Zhu, Y. J. & Jiao, R. Z. (1996). *Sep. Sci. Technol.* **31**, 2723–2731.

Choppin, G. R. (2002). *J. Alloys Compd.* **344**, 55–59.

Cowie, B. E., Purkis, J. M., Austin, J., Love, J. B. & Arnold, P. L. (2019). *Chem. Rev.* **119**, 10595–10637.

Cross, J. N., Macor, J. A., Bertke, J. A., Ferrier, M. G., Girolami, G. S., Kozimor, S. A., Maassen, J. R., Scott, B. L., Shuh, D. K., Stein, B. W. & Stieber, S. C. (2016). *Angew. Chem. Int. Ed.* **55**, 12755–12759.

Cross, J. N., Su, J., Batista, E. R., Cary, S. K., Evans, W. J., Kozimor, S. A., Mocko, V., Scott, B. L., Stein, B. W., Windorff, C. J. & Yang, P. (2017). *J. Am. Chem. Soc.* **139**, 8667–8677.

Daly, S. R., Keith, J. M., Batista, E. R., Boland, K. S., Clark, D. L., Kozimor, S. A. & Martin, R. L. (2012). *J. Am. Chem. Soc.* **134**, 14408–14422.

Daly, S. R., Keith, J. M., Batista, E. R., Boland, K. S., Kozimor, S. A., Martin, R. L. & Scott, B. L. (2012). *Inorg. Chem.* **51**, 7551–7560.

Daly, S. R., Klaehn, J. R., Boland, K. S., Kozimor, S. A., MacInnes, M. M., Peterman, D. R. & Scott, B. L. (2012). *Dalton Trans.* **41**, 2163–2175.

Denning, R. G. (1992). *Complexes, Clusters and Crystal Chemistry*, pp. 215–276. Berlin, Heidelberg: Springer.

Denning, R. G. (2007). *J. Phys. Chem. A*, **111**, 4125–4143.

Denning, R. G., Green, J. C., Hutchings, T. E., Dallera, C., Tagliaferri, A., Giarda, K., Brookes, N. B. & Braicovich, L. (2002). *J. Chem. Phys.* **117**, 8008–8020.

Diamond, R. M., Street, K. & Seaborg, G. T. (1954). *J. Am. Chem. Soc.* **76**, 1461–1469.

Dolomanov, O. V., Bourhis, L. J., Gildea, R. J., Howard, J. A. K. & Puschmann, H. (2009). *J. Appl. Cryst.* **42**, 339–341.

Donahue, C. M., Lezama Pacheco, J. S., Keith, J. M. & Daly, S. R. (2014). *Dalton Trans.* **43**, 9189–9201.

Faas, S., Snijders, J. G., van Lenthe, J. H., van Lenthe, E. & Baerends, E. J. (1995). *Chem. Phys. Lett.* **246**, 632–640.

Gaunt, A. J., Reilly, S. D., Enriquez, A. E., Scott, B. L., Ibers, J. A., Sekar, P., Ingram, K. I., Kaltsoyannis, N. & Neu, M. P. (2008). *Inorg. Chem.* **47**, 29–41.

George, G. N. (2001). *EDG_FIT*. Stanford Synchrotron Radiation Laboratory, Stanford Linear Accelerator Center: Stanford, CA, USA.

Greer, R. D. M., Celis-Barros, C., Sperling, J. M., Gaiser, A. N., Windorff, C. J. & Albrecht-Schönzart, T. E. (2020). *Inorg. Chem.* **59**, 16291–16300.

Ha, Y., Arnold, A. R., Nuñez, N. N., Bartels, P. L., Zhou, A., David, S. S., Barton, J. K., Hedman, B., Hodgson, K. O. & Solomon, E. I. (2017). *J. Am. Chem. Soc.* **139**, 11434–11442.

Ingram, K. I., Tassell, M. J., Gaunt, A. J. & Kaltsoyannis, N. (2008). *Inorg. Chem.* **47**, 7824–7833.

Jensen, M. P. & Bond, A. H. (2002). *J. Am. Chem. Soc.* **124**, 9870–9877.

Kaneko, M., Miyashita, S. & Nakashima, S. (2015). *Inorg. Chem.* **54**, 7103–7109.

Kaneko, M. & Watanabe, M. (2018). *J. Radioanal. Nucl. Chem.* **316**, 1129–1137.

Kaneko, M., Watanabe, M., Miyashita, S. & Nakashima, S. (2017). *J. Nucl. Radiochem. Sci.* **17**, 9–15.

Keith, J. M. & Batista, E. R. (2012). *Inorg. Chem.* **51**, 13–15.

Kozimor, S. A., Yang, P., Batista, E. R., Boland, K. S., Burns, C. J., Christensen, C. N., Clark, D. L., Conradson, S. D., Hay, P. J., Lezama, J. S., Martin, R. L., Schwarz, D. E., Wilkerson, M. P. & Wolfsberg, L. E. (2008). *Inorg. Chem.* **47**, 5365–5371.

Kozimor, S. A., Yang, P., Batista, E. R., Boland, K. S., Burns, C. J., Clark, D. L., Conradson, S. D., Martin, R. L., Wilkerson, M. P. & Wolfsberg, L. E. (2009). *J. Am. Chem. Soc.* **131**, 12125–12136.

Lan, J. H., Shi, W. Q., Yuan, L. Y., Li, J., Zhao, Y. L. & Chai, Z. F. (2012). *Coord. Chem. Rev.* **256**, 1406–1417.

Leavitt, C. M., Gresham, G. L., Benson, M. T., Gaumet, J. J., Peterman, D. R., Klaehn, J. R., Moser, M., Aubriet, F., Van Stipdonk, M. J. & Groenewold, G. S. (2008). *Inorg. Chem.* **47**, 3056–3064.

Lee, C., Yang, W. & Parr, R. G. (1988). *Phys. Rev. B*, **37**, 785–789.

Lee, K., Blake, A. V., Donahue, C. M., Spielvogel, K. D., Bellott, B. J. & Daly, S. R. (2019). *Angew. Chem. Int. Ed.* **58**, 12451–12455.

Lehman-Andino, I., Su, J., Papathanasiou, K. E., Eaton, T. M., Jian, J., Dan, D., Albrecht-Schmitt, T. E., Dares, C. J., Batista, E. R., Yang, P., Gibson, J. K. & Kavallieratos, K. (2019). *Chem. Commun.* **55**, 2441–2444.

Löble, M. W., Keith, J. M., Altman, A. B., Stieber, S. C., Batista, E. R., Boland, K. S., Conradson, S. D., Clark, D. L., Lezama Pacheco, J., Kozimor, S. A., Martin, R. L., Minasian, S. G., Olson, A. C., Scott, B. L., Shuh, D. K., Tyliszczak, T., Wilkerson, M. P. & Zehnder, R. A. (2015). *J. Am. Chem. Soc.* **137**, 2506–2523.

Martin, R. L. & Shirley, D. A. (1977). *Electron Spectroscopy, Theory, Techniques and Applications*, Vol. 1, edited by C. R. Brundle & A. D. Baker, pp. 75–117. London: Academic Press.

Meng, D. C., Pu, N., Mei, L., Sun, T. X., Xu, L., Shi, W. Q., Chen, J. & Xu, C. (2018). *J. Radioanal. Nucl. Chem.* **317**, 121–129.

Minasian, S. G., Batista, E. R., Booth, C. H., Clark, D. L., Keith, J. M., Kozimor, S. A., Lukens, W. W., Martin, R. L., Shuh, D. K., Stieber, S. C. E., Tylisczcak, T. & Wen, X. D. (2017). *J. Am. Chem. Soc.* **139**, 18052–18064.

Minasian, S. G., Keith, J. M., Batista, E. R., Boland, K. S., Clark, D. L., Conradson, S. D., Kozimor, S. A., Martin, R. L., Schwarz, D. E., Shuh, D. K., Wagner, G. L., Wilkerson, M. P., Wolfsberg, L. E. & Yang, P. (2012). *J. Am. Chem. Soc.* **134**, 5586–5597.

Minasian, S. G., Keith, J. M., Batista, E. R., Boland, K. S., Clark, D. L., Kozimor, S. A., Martin, R. L., Shuh, D. K. & Tyliszczak, T. (2014). *Chem. Sci.* **5**, 351–359.

Minasian, S. G., Keith, J. M., Batista, E. R., Boland, K. S., Kozimor, S. A., Martin, R. L., Shuh, D. K., Tyliszczak, T. & Vernon, L. J. (2013). *J. Am. Chem. Soc.* **135**, 14731–14740.

Mulliken, R. S. (1955). *J. Chem. Phys.* **23**, 1833–1840.

Pemmaraju, C. D., Copping, R., Wang, S., Janousch, M., Teat, S. J., Tyliszczak, T., Canning, A., Shuh, D. K. & Prendergast, D. (2014). *Inorg. Chem.* **53**, 11415–11425.

Pepper, M. & Bursten, B. E. (1991). *Chem. Rev.* **91**, 719–741.

Peterman, D. R., Greenhalgh, M. R., Tillotson, R. D., Klaehn, J. R., Harrup, M. K., Luther, T. A. & Law, J. D. (2010). *Sep. Sci. Technol.* **45**, 1711–1717.

Peterman, D. R., Martin, L. R., Klaehn, J. R., Harrup, M. K., Greenhalgh, M. R. & Luther, T. A. (2009). *J. Radioanal. Nucl. Chem.* **282**, 527–531.

Pinkerton, A. A., Ahlers, F. P., Greiwing, H. F. & Krebs, B. (1997). *Inorg. Chim. Acta*, **257**, 77–81.

Pu, N., Su, J., Xu, L., Sun, T., Batista, E. R., Chen, J., Yang, P., Shafer, J. C. & Xu, C. (2020). *Inorg. Chem.* **59**, 161–171.

Pu, N., Xu, L., Sun, T. X., Chen, J. & Xu, C. (2019). *J. Radioanal. Nucl. Chem.* **320**, 219–226.

Queen, M. S., Towey, B. D., Murray, K. A., Veldkamp, B. S., Byker, H. J. & Szilagyi, R. K. (2013). *Coord. Chem. Rev.* **257**, 564–578.

Ravel, B. & Newville, M. (2005). *J. Synchrotron Rad.* **12**, 537–541.

Rigaku Oxfrod Diffraction (2018). *CrysAlisPro*, https://www.rigaku.com/products/crystallography/crysalis.

Rose, K., Shadle, S. E., Glaser, T., de Vries, S., Cherepanov, A., Canters, G. W., Hedman, B., Hodgson, K. O. & Solomon, E. I. (1999). *J. Am. Chem. Soc.* **121**, 2353–2363.

Sadhu, B. & Dolg, M. (2019). *Inorg. Chem.* **58**, 9738–9748.

Sarangi, R., DeBeer George, S., Rudd, D. J., Szilagyi, R. K., Ribas, X., Rovira, C., Almeida, M., Hodgson, K. O., Hedman, B. & Solomon, E. I. (2007). *J. Am. Chem. Soc.* **129**, 2316–2326.

Segala, M. & Chong, D. P. (2010). *J. Electron Spectrosc. Relat. Phenom.* **182**, 141–144.

Shadle, S. E., Penner-Hahn, J. E., Schugar, H. J., Hedman, B., Hodgson, K. O. & Solomon, E. I. (1993). *J. Am. Chem. Soc.* **115**, 767–776.

Sheldrick, G. M. (2008). *Acta Cryst.* A**64**, 112–122.

Smiles, D. E., Batista, E. R., Booth, C. H., Clark, D. L., Keith, J. M., Kozimor, S. A., Martin, R. L., Minasian, S. G., Shuh, D. K., Stieber, S. C. E. & Tyliszczak, T. (2020). *Chem. Sci.* **11**, 2796–2809.

Solomon, E. I., Hedman, B., Hodgson, K. O., Dey, A. & Szilagyi, R. K. (2005). *Coord. Chem. Rev.* **249**, 97–129.

Spencer, L. P., Yang, P., Minasian, S. G., Jilek, R. E., Batista, E. R., Boland, K. S., Boncella, J. M., Conradson, S. D., Clark, D. L., Hayton, T. W., Kozimor, S. A., Martin, R. L., MacInnes, M. M., Olson, A. C., Scott, B. L., Shuh, D. K. & Wilkerson, M. P. (2013). *J. Am. Chem. Soc.* **135**, 2279–2290.

Storey, A. E., Zonnevijlle, F., Pinkerton, A. A. & Schwarzenbach, D. (1983). *Inorg. Chim. Acta*, **75**, 103–113.

Su, J., Batista, E. R., Boland, K. S., Bone, S. E., Bradley, J. A., Cary, S. K., Clark, D. L., Conradson, S. D., Ditter, A. S., Kaltsoyannis, N., Keith, J. M., Kerridge, A., Kozimor, S. A., Löble, M. W., Martin, R. L., Minasian, S. G., Mocko, V., La Pierre, H. S., Seidler, G. T., Shuh, D. K., Wilkerson, M. P., Wolfsberg, L. E. & Yang, P. (2018). *J. Am. Chem. Soc.* **140**, 17977–17984.

Sun, N., Dey, A., Xiao, Z., Wedd, A. G., Hodgson, K. O., Hedman, B. & Solomon, E. I. (2010). *J. Am. Chem. Soc.* **132**, 12639–12647.

Szilagyi, R. K., Lim, B. S., Glaser, T., Holm, R. H., Hedman, B., Hodgson, K. O. & Solomon, E. I. (2003). *J. Am. Chem. Soc.* **125**, 9158–9169.

Tian, G., Zhu, Y., Xu, J., Zhang, P., Hu, T., Xie, Y. & Zhang, J. (2003). *Inorg. Chem.* **42**, 735–741.

Tian, G. X., Zhu, Y. J., Xu, J. M., Hu, T. D. & Xie, Y. N. (2002). *J. Alloys Compd.* **334**, 86–91.

Velde, G. te, Bickelhaupt, F. M., Baerends, E. J., Fonseca Guerra, C., van Gisbergen, S. J. A., Snijders, J. G. & Ziegler, T. (2001). *J. Comput. Chem.* **22**, 931–967.

Wang, F., Jia, C. & Chen, J. (2013). *J. Radioanal. Nucl. Chem.* **298**, 531–536.

Wang, F., Jia, C., Pan, D. F. & Chen, J. (2013). *Ind. Eng. Chem. Res.* **52**, 18373–18378.

Wang, Z., Pu, N., Tian, Y., Xu, C., Wang, F., Liu, Y., Zhang, L., Chen, J. & Ding, S. (2019). *Inorg. Chem.* **58**, 5457–5467.

Weigl, M., Denecke, M. A., Panak, P. J., Geist, A. & Gompper, K. (2005). *Dalton Trans.* **34**, 1281–1286.

Xu, C. & Rao, L. (2014). *Chem. Eur. J.* **20**, 14807–14815.

Xu, Q. C., Wu, J. F., Chang, Y. Z., Zhang, L. X. & Yang, Y. S. (2008). *Radiochim. Acta*, **96**, 771–779.

Zheng, L., Zhao, Y. D., Tang, K., Ma, C. Y., Hong, C. H., Han, Y., Cui, M. Q. & Guo, Z. Y. (2014). *At. Spectrosc.* **101**, 1–5.